

Motion corrected abdominal PET/MRI using MR-based motion tracking

Stan Meinders¹

Abstract — Respiratory and bulk motion in abdominal PET studies lead to blurring of PET reconstructions. As a result, lesion volumes tend to be overestimated, while tracer uptake is underestimated and small lesions become undetectable. Motion correction may be used to correct PET images that would otherwise be blurred by motion. The purpose of this study is to investigate the feasibility of using MR-based motion tracking for motion correction on abdominal PET images acquired with PET/MRI. To study this, motion vector fields were generated using the novel MR sequence rCASPR. These vector fields were subsequently applied to simulated PET data acquired with the digital XCAT phantom. Motion correction of the reconstructions was done using the CASToR reconstruction framework complemented with a motion correction method based on deformation vector fields. The influence of only using either respiratory or bulk motion correction was studied on a simulation with both respiratory and bulk motion. The feasibility of using MR-based motion tracking with the rCASPR technique for motion correction of PET simulations was shown. Higher CRC values, CNR values and maximum uptake values and lower lesion volumes were found for the reconstruction with full motion correction than for the reconstruction without motion correction. Moreover, the relative impact of bulk motion correction versus respiratory motion correction could be assessed in this PET simulation containing both respiratory and bulk motion.

Index Terms — Motion correction, PET/MRI

I. INTRODUCTION

Positron emission tomography (PET) is an imaging modality which is commonly used in oncology. In PET studies, a positron emitting tracer is injected into a patient. These tracers undergo radioactive decay, which results in the emission of a positron. Combined with an electron, annihilation takes place resulting in two gamma photons with a 180° opposing direction. If these photons are detected nearly simultaneously (i.e. within a small time window) in two opposing detectors, this is stored as a coincidence, which is used for the reconstruction of the PET image. Depending on the tracer, several physiological processes can be imaged using PET. Most common in oncology is the use of 18-fluorodeoxyglucose (FDG), which can be used to study the glucose metabolism (Papathanassiou et al. 2009).

Abdominal PET images may be subject to respiratory motion, which affects the accuracy of the detection of lesions on PET images. Due to the blurring caused by motion, the volume of lesions tends to be overestimated, while the tracer uptake is underestimated. Moreover, the visibility of small lesions is

reduced on images affected by motion (Catana, 2015). Apart from respiratory motion, blurring may occur as a result of repositioning of the patient. This is mainly seen in pediatric PET studies if the patient has not been anesthetized to prevent them from moving.

This study focuses on correcting PET images for liver motion. In adults, the liver motion during free breathing is typically in the order of 10 mm in the left-right and anterior-posterior direction, and 10-26 mm in the feet-head direction. During deep breathing, the liver can move up to 75 mm in the feet-head direction. These motions are mainly rigid, but small nonrigid deformations of up to 10 mm have been reported as well (Catana, 2015). Considering that the resolution of PET studies is often 3-5 mm, this motion is likely to cause blurring in the images.

Currently, Oncofreeze AI, developed by Siemens Healthineers, can be used to correct for respiratory motion without the need of an external gating device. Based on the raw PET list-mode data, it derives a respiratory signal which is used for respiratory gating. Subsequently, motion is estimated from the gated PET images and this motion estimation is used for a motion corrected PET reconstruction. Other types of motion such as bulk motion cannot be corrected for with this method (Siemens Healthineers, 2021).

With the relatively recent development of integrated whole body PET/MRI systems, new opportunities for motion correction of PET images have been presented. Similar to PET/CT, PET/MRI combines the information of physiological functionality provided by PET with anatomical information from magnetic resonance imaging (MRI) (or computed tomography (CT) in PET/CT) (Ehman et al., 2017). Depending on the MR sequence that is simultaneously used during the PET acquisition, several types of motion can be estimated. Methods for MR-based motion correction of PET images have been reported for head motion, respiratory motion, cardiac motion and dual cardiac and respiratory motion (Catana, 2018). A novel 3D method to estimate motion from MR data is rCASPR. rCASPR was used in this study for motion correction with PET/MRI.

This study is part of the development of a PET/MRI scanner at the UMC Utrecht. It continues on the work of Van der Schagt (2021), who implemented a method to correct for motion with deformation vector fields. Feasibility of this method was shown for PET reconstructions with simulated vector fields and without other corrections. The aim of this study is to investigate the feasibility of using real-world MR-based vector fields generated with rCASPR for correction of both respiratory

¹ Student of the Master's programme Medical Imaging at Utrecht University; Research Intern at the department of Radiotherapy at the UMC Utrecht under supervision of dr. ir. C. Beijst

motion and repositioning of the patient. Additionally, attenuation and scatter correction are incorporated in this study. Apart from studying the feasibility, the impact of only using either bulk or respiratory motion correction is studied. To investigate this, the detection and quantification of lesions in the liver is studied.

The rest of this report is organized as follows. The rCASPR technique and the iterative PET reconstruction framework with motion correction and other corrections are described in section II. The used methods for the generation of motion vector fields with rCASPR are described in section III. Furthermore, details of the simulation, reconstruction and analysis of the PET data are described there. In section IV, the results of the experiments are shown and finally in section V, these results are discussed and conclusions are drawn.

II. THEORY

II. A. MR-based motion estimation

1) Current status in PET/MRI

Most methods currently developed for motion correction in PET/MRI are specific for one type of motion (e.g. respiratory motion, cardiac motion, head motion) or dual respiratory and cardiac motion (Catana, 2018). In abdominal PET/MRI, respiratory and bulk motion are the two types of motion which are observed predominantly. Therefore, a combined approach which is both able to correct for respiratory motion as well as bulk motion provides significant improvement for abdominal PET/MRI. Marin et al. (2020) have reported such a method in which they use a subspace-based MR imaging method with highly undersampled k -space data, using a temporal resolution of 9.5 volumes per second. Motion estimation was done in three steps. First, the data was binned in several bulk motion frames by visual determination. Subsequently, each bulk motion frame was binned into respiratory frames by tracking the position of the tip of the right liver lobe. Lastly, a reconstruction was made for all bins and motion was estimated by registering the MR images. Limitations for this method, however, were the high computation time and distorted MR images during the repositioning. These distorted images could not be used to generate deformation fields, which resulted in discarding the PET data belonging to the frames of the bulk movement (Marin et al., 2020).

2) T_1 -w rCASPR

A novel method for MR-based motion estimation is rCASPR (rebound Cartesian Acquisition with Spiral PRofile ordering), which uses image-based motion estimation. This method was originally developed for motion tracking in MR-guided radiotherapy. rCASPR uses rotating Cartesian spiral interleaves which both start and end at the periphery as sampling trajectory, as shown in Figure 1. Sampling is done using a turbo spin echo pulse sequence. Self-navigation with repeated $k_{y,z} = (0,0)$ phase encodes is used for estimation of the respiratory motion (Bruijnen et al., 2022).

During the reconstruction, the k -space data is first cropped to a lower spatial resolution and secondly the data is sorted in a number of respiratory frames using the self-navigation signal. Subsequently, images are reconstructed for each respiratory

frame and interpolated to a higher resolution. Lastly, deformation vector fields are generated using registration to a reference position (e.g. the exhale position) (Bruijnen et al., 2022). In this study, a T_1 -weighted version of rCASPR was used.

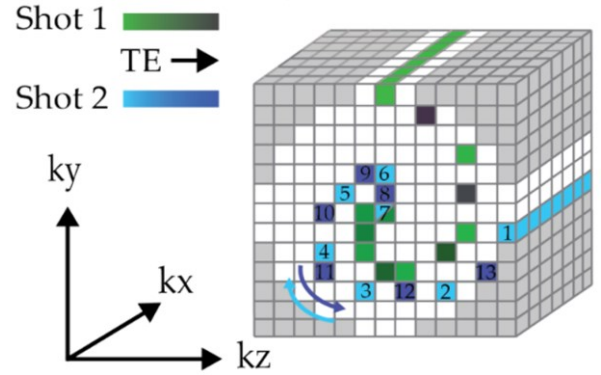


Figure 1: Sampling trajectory that is used by rCASPR. Following the blue trajectory, it can be seen that the phase encodes first moves inwards (numbers 1-7) and then moves outwards again by sampling phase encodes between the inwards phase encodes (numbers 7-13). This is done repetitively with rotating spirals to sample the full k -space cylinder in white (with an undersampling factor) (Bruijnen et al., 2022).

II. B. PET reconstruction

1) Iterative PET reconstruction

PET images are reconstructed using iterative reconstruction methods. A commonly used algorithm in clinical practice is the ordered subsets expectation maximization (OSEM) algorithm, which is a modified version of the maximum likelihood expectation maximization (ML-EM) algorithm. In ML-EM, an image guess is forward projected to the projection domain. This set of projections is compared with the measured projections to obtain correction factors for each projection. These correction factors are backprojected to the image domain, which is subsequently used to update the image guess. This updated image guess is used in the next iteration. By doing multiple iterations, an accurately reconstructed image is formed. A pseudo code for this algorithm can be found in Figure 3. The OSEM algorithm is similar to ML-EM, but each iteration is divided into several subsets. These subsets contain a part of the full dataset and the image guess is updated using only this part of the data for each subset. In this way, the image guess is updated multiple times during one iteration, which reduces reconstruction time (Alessio & Kinahan, 2006).

2) Correction factors in PET reconstruction

In PET imaging, corrections are required to obtain quantitative PET images. These corrections include attenuation correction, scatter correction, random correction and normalization. These corrections can be applied either prior to or during the iterative reconstruction process (Tong et al., 2010).

a) Attenuation correction

Applying attenuation correction usually leads to the biggest improvement of image quality. Attenuation correction is required since the annihilation photons interact with human

tissue, which affects the probability that an event is detected. The effect of attenuation varies regionally in PET reconstructions, which may result in artifacts and explains the need for attenuation correction (Zaidi et al., 2007). Correcting for attenuation is usually done by generating an attenuation map containing linear attenuation coefficients for each voxel. This map is used to get the expected attenuation for each line of response (Tong et al., 2010). In PET/MRI, these maps are commonly generated from the MR images using a priori knowledge about attenuation in different tissue types (Delso & Nuyts, 2018).

b) Scatter correction

Apart from true coincidences, scatter and random coincidences are detected in PET studies. Scatter coincidences are detected when one or both photons from the annihilation event are scattered, which leads to an incorrect positioning of the event, as shown in Figure 2. Heavily scattered photons can be filtered from the data by using an energy threshold, but events resulting from less heavily scattered photons cannot and these events should be corrected for (Tong et al., 2010). A commonly used approach to correct for scatters is single scatter simulation (SSS), which simulates the amount of scattered coincidences expected for a given scanner geometry, attenuation map and activity map (Watson, 2000). For this study, an SSS algorithm for the PET/MRI system at the UMC Utrecht was developed (unpublished data, Meinders & Jose Santo, 2022). Further information on this SSS algorithm can be found in Appendix 1.

c) Random correction

As shown in Figure 2, random coincidences result from two photons of two separate annihilation events. These coincidences reduce image contrast and can introduce image artifacts. Correction is usually done by estimating a random event sinogram (Tong et al., 2010). The random events can be estimated either by using the delayed event subtraction method or by estimation using the singles data (Cherry, 2012). In this study, random coincidences are neglected.

d) Normalization

One last correction that is usually incorporated in PET reconstructions is normalization. This is done to correct for variations in detector efficiency (Tong et al., 2010) and to correct for spatially varying sensitivity (Cherry, 2012). In this study, normalization for detector efficiency was set to unity for all voxels.

3) Motion correction with iterative PET reconstruction

During the iterative process of PET reconstructions, motion correction based on deformation vector fields can be performed, as shown by Van der Schagt (2021). The method developed by Van der Schagt combines the OSEM algorithm in CASToR (Merlin et al., 2018) with motion correction based on deformation vector fields.

The reconstruction method splits every iteration in multiple subsets. Each subset is split into the different motion frames and for each frame, the image guess is deformed using the deformation vector field corresponding to the frame, after which it is forward projected. These projections are compared with the measured projections of the given frame and based on this comparison, an error image is reconstructed using backprojection. Subsequently, the image guess is updated with the error image and deformed back to the reference frame. By using deformation vector fields, this method is able to correct for any type of motion. A limitation of this method, however, is the computational time and high memory usage when vector fields with high frequencies are used (Van der Schagt, 2021). The pseudo code of this algorithm is shown in Figure 3.

This computational limitation can partially be overcome if the motion is periodic (e.g. respiratory motion). As discussed, rCASPR uses binning of the data into a number of respiratory frames to correct for respiratory motion, exploiting the knowledge that respiratory motion is periodic. Since the PET and MR data will be acquired simultaneously in PET/MRI, this same binning can be done for the PET data. In this way, the PET data can still be corrected for motion with a high temporal resolution, without extremely long computational times.

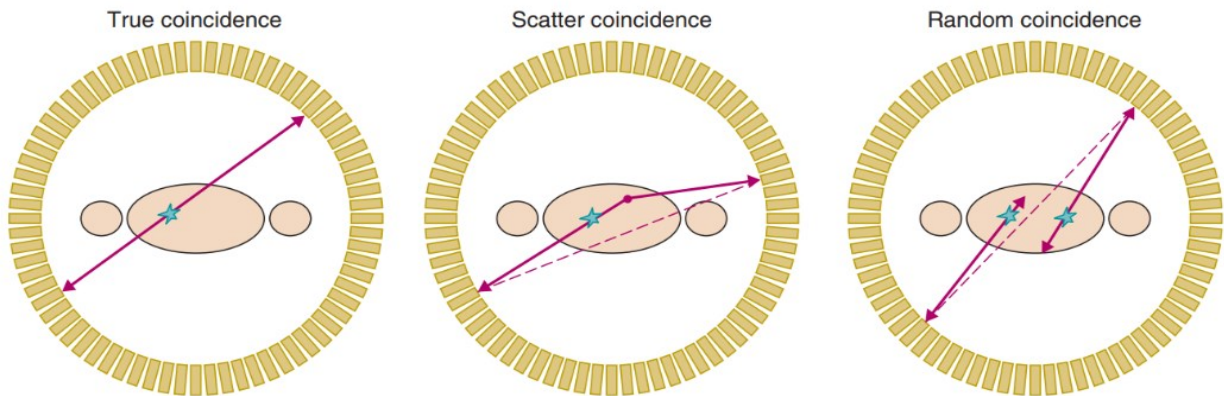


Figure 2: The differences between true, scatter and random coincidences. As shown, scatter and random coincidences result in incorrect positioning of the event, which shows the need for correction of these coincidences (Cherry, 2012).

OSEM iterative algorithm

Black = normal iterative algorithm

Gray = extra steps for motion correction

For nr_iterations:

For nr_subsets:

For nr_deformations:

- Deform image guess with corresponding vector field
- Forward project image guess -> projections
- Compare projections with measured projections (part of measured projections corresponding to used vector field)
- Back project the error projections
- Update guess image with error image
- Deform back the guess image

Figure 3: Pseudocode for iterative PET reconstructions with vector field based motion correction (Van der Schagt, 2021).

III. MATERIALS AND METHODS

The purpose of this study was to investigate the feasibility of using rCASPR for motion correction in PET/MRI. To study this, MR-based vector fields were acquired from an rCASPR scan of a healthy volunteer and applied to simulated PET data. The reconstructions of the PET data were analyzed by their accuracy of the detection and quantification of liver lesions.

III. A. MR vector fields

1) rCASPR acquisition

For the generation of the MR-based vector fields, a healthy adult volunteer was scanned using the rCASPR sequence. During the acquisition, the volunteer was asked to breathe normally and to move 1-2 cm to the right or left several times during the acquisition. The 1.5T Elekta Unity/Philips Marlin was used. This is representative for PET/MRI studies in the UMC Utrecht, since the PET/MRI system at the UMC Utrecht also features a 1.5T magnet, a split gradient coil and an identical body coil. The MR settings can be found in Table 1.

2) rCASPR reconstruction

For the reconstruction, the rCASPR data was first prewhitened and coil compressed by using the coil sensitivity maps and noise levels generated from a reference scan. The self-navigation signals of the different coil channels were clustered and used to bin the preprocessed data into 20 respiratory phases using a soft-gating method. With soft-gating, data from neighboring phases is added to a phase by weighting each phase (Jiang et al., 2018). A Gaussian kernel was used for the soft-gating. Subsequently, the spatial resolution was reduced to $5.0 \times 5.0 \times 5.0 \text{ mm}^3$ by cropping the k -space data (Bruijnen et al., 2022).

Using parallel imaging and compressed sensing with locally low-rank constraints, respiratory resolved images were obtained. These low-rank constraints are used to better deal

with aliasing artifacts in low-resolution images (Jiang et al., 2018). Subsequently, the low-resolution respiratory resolved images were interpolated in order to obtain the original high spatial resolution. Using registration with the optical flow algorithm (Zachiu et al., 2015), deformation vector fields were obtained for each respiratory phase taking the exhale position as reference. The same registration was performed in the opposing direction to obtain the backward deformation vector fields. Lastly, these forward and backward vector fields were postprocessed to be consistent with each other (Bruijnen et al., 2022).

Afterwards, a new reconstruction of the same k -space data was made using a dynamic reconstruction with 10 dynamics. This was done by splitting the data into 10 consecutive frames with the same frame length. The different dynamics were reconstructed using parallel imaging and compressed sensing. Vector fields were generated for each dynamic with respect to the reference image of the respiratory resolved reconstruction by registration with the optical flow algorithm (Zachiu et al., 2015).

The motion vector fields that are defined as the gold standard for the subsequent simulations were created by combining the respiratory and dynamic vector fields. Each dynamic was binned into the observed respiratory frames in that dynamic. Subsequently, by linear addition, the respiratory and dynamic vector fields were combined for each observed combination of respiratory and dynamic frame.

Table 1: Scanner and sequence parameters of the MR acquisition used for obtaining motion vector fields.

Setting	T1-w rCASPR
Spatial resolution	$2.0 \times 2.0 \times 2.0 \text{ mm}^3$
FOV	$300 \times 229.3 \times 319 \text{ mm}^3$
Dimensions	$150 \times 115 \times 160$
Repetition time	4.7 ms
Echo time	2.1 ms
Flip angle	20°
Readout bandwidth	434.8 Hz
TSE factor	55
Coils (#Channels)	Anterior + Posterior (8)
Trajectory	Cartesian rewind spirals
Scan time	132.4 s
Temporal resolution	3.9 Hz (258.5 ms per dynamic)
Scanner	1.5T Elekta Unity/Philips Marlin

III. B. Simulated 4D PET data

To simulate PET data, the digital XCAT phantom was used to obtain an activity and attenuation map with the anatomy of a 50-year-old woman (Segars et al., 2010). Using affine registration followed by nonrigid registration with the *elastix* software (Klein et al., 2009; Shamonin et al., 2014), the phantom activity and attenuation map were transformed to

resemble the anatomy of the MR reference image. By applying the inverse MR-based vector fields on the transformed activity map using MATLABs built in *imwarp* function, a 4D activity map was generated of a moving phantom. Three spherical lesions with a radius of 7.5, 5.0 and 3.3 mm were added, located in a middle slice of the liver, as shown in Figure 4. The lesions had an activity 3.5 times higher than the liver.

This 4D activity map was converted to list-mode true events with an analytical projector provided by the makers of the CASToR framework, complemented with the geometry of the PET/MRI system at the UMC Utrecht. This simulation was done for one bed position. For the experiment, it was assumed that 125,000 true events should be detected per second, as is common in PET acquisitions at the UMC Utrecht. This resulted in a total of 16.5×10^6 true events. Attenuation was taken into account during the generation of the true events. Scatter events were added using a single scatter simulation (SSS) algorithm (Watson, 2000). The input for the SSS were the 4D activity and attenuation map of the phantom and the used scatter-to-true ratio was 1.0, as is common for abdominal 3D PET scans (Cherry et al., 2012). Poisson noise was added to the simulated events. This procedure resulted in the simulated list-mode data that was regarded as the gold standard for the subsequent simulations and reconstructions.

III. C. PET reconstruction

PET reconstructions were performed using the CASToR framework (Merlin et al., 2018) complemented with the vector field motion correction method developed by Van der Schagt (2021). Attenuation correction was performed using the transformed attenuation map of the XCAT phantom for each frame to compute the attenuation correction factors for each line of response. Scatter correction was performed using SSS for each timeframe in the used vector field for motion correction. Other reconstruction settings can be found in Table 2.

Reconstructions of the PET simulation with the rCASPR vector fields were performed using no motion correction, motion correction with only the respiratory vector fields, motion correction with only the dynamic vector fields and

motion correction with the combined vector fields. For the motion corrected reconstruction with the combined vector field, scatter correction with SSS was done on 20 frames which were obtained by dividing each dynamic frame in two smaller frames with equal size. All reconstructions were blurred using a 3D Gaussian postreconstruction kernel with a standard deviation of 1.5 mm using the *imgaussfilt3* function in MATLAB.

Table 2: Reconstruction parameters of the PET reconstructions.

Parameter	
Spatial resolution	3.0 x 3.0 x 3.0 mm ³
FOV	460 x 460 x 148 mm ³
Dimensions	153 x 153 x 50
Optimizer	ML-EM
Number of iterations & subsets	4:21
Projector	Classic Siddon

III. D. Quantitative analysis

The four reconstructions (i.e. no motion correction, respiratory motion correction, bulk motion correction and full motion correction) of the simulations with the rCASPR-based vector fields were analyzed based on the maximum uptake value, the volume, the contrast recovery coefficient (CRC) and the contrast-to-noise ratio (CNR) of the lesions. To investigate the impact of both different types of motion (i.e. bulk and respiratory motion), the values were compared to the full motion corrected reconstruction, since that reconstruction was made with the PET data defined as gold standard.

First of all, the maximum uptake value of each reconstruction was obtained and the average uptake value in the liver was calculated incorporating the slices where lesions were observed. Based on the maximum uptake value and the average uptake value in the liver, lesions were defined using a threshold

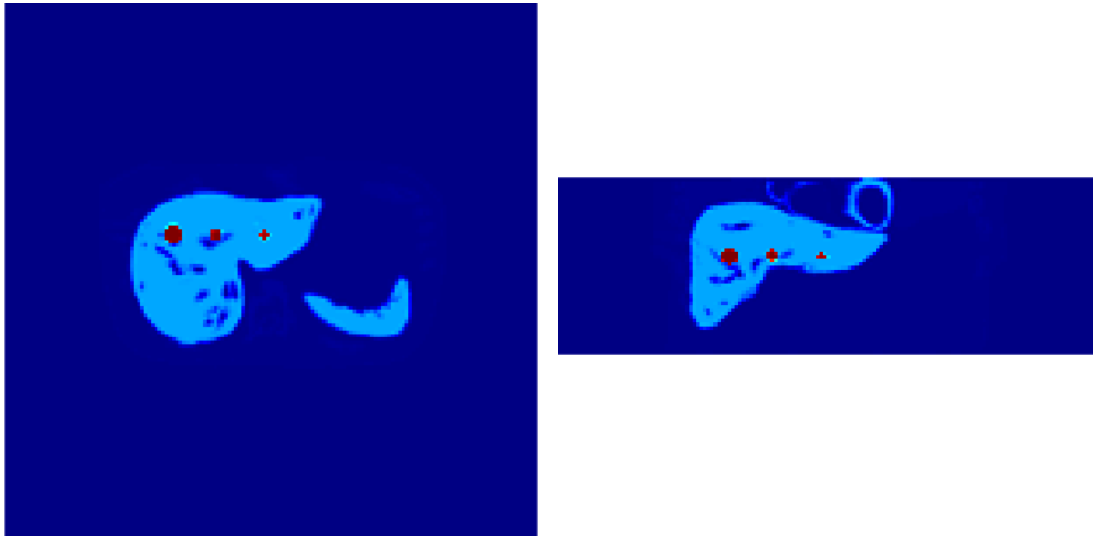


Figure 4: Axial (left) and coronal (right) view of the simulated lesions in the liver of the XCAT-phantom.

and a combined edge- and surface-based connected component analysis. The used threshold was defined by

$$T = \mu_{liver} + 1/2 * (max_{voxel} - \mu_{liver}) \text{ (Eq. 1),}$$

where μ_{liver} is the average value in the liver and max_{voxel} is the maximum uptake value in the reconstruction. Lesions needed to consist of at least two voxels in order to exclude noise. For each segmented lesion, the maximum uptake value was obtained.

The CRC was calculated by

$$CRC = \frac{(\mu_{lesion}/\mu_{liver}) - 1}{C_{simulated} - 1} \text{ (Eq. 2)}$$

where μ_{lesion} and μ_{liver} are the mean uptake values in the spherical regions of interest and the liver. $C_{simulated}$ is the simulated contrast between the lesions and the liver.

The CNR was calculated for all regions of simulated lesions by

$$CNR = \frac{\mu_{lesion} - \mu_{liver}}{\sigma_{liver}} \text{ (Eq. 3).}$$

Here, μ_{lesion} is the mean uptake value of the spherical regions of interest, μ_{liver} is the mean uptake value of the liver and σ_{liver} is the standard deviation of the uptake values in the liver.

IV. RESULTS

1) Quantification of the detected motion

For all three spherical regions of interest, the maximum displacement was obtained in all three directions. These values are summarized in Table 3. Figure 5 shows a visualization of the obtained vector fields.

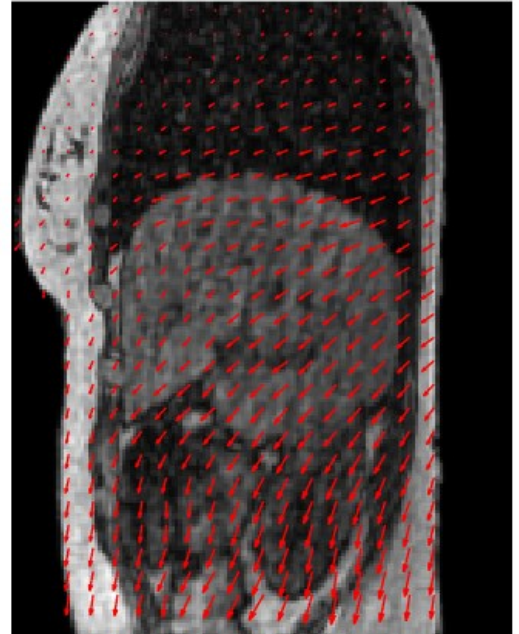
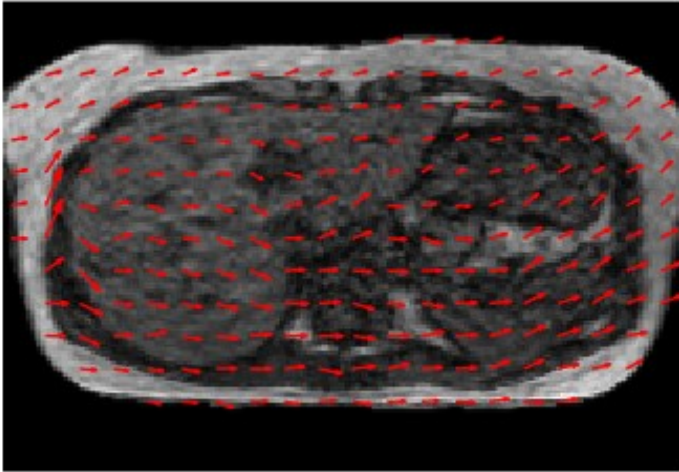


Figure 5: A visualization of the obtained vector fields overlaid at the reference frame. Left shows the axial view and right shows the sagittal view.

2) Quantitative analysis reconstructions

A visual comparison of the middle axial slice through the lesions is shown in Figure 6 and a comparison of two coronal slices of the four different reconstructions is shown in Figure 7.

Three different lesions were simulated in these slices. The 7.5 mm lesion is for all three reconstructions clearly visible. The 5.0 mm lesion is visible as well, although it appears less intense for the reconstruction without motion correction. The 3.3 mm lesion in the right lobe of the liver is less clearly detectable on all reconstructions. The 5.0 mm lesion is a good example where the effect of motion correction can be seen from these comparisons. In Figure 7, for the reconstruction with the bulk and combined vector fields, the highest intensity of the middle lesion can be seen in the middle slice through the lesions (left), whereas this is observed in the adjacent posterior slice (right) for the reconstructions with respiratory motion correction and without motion correction. Note that these differences are minimal due to the small displacements in the obtained MR-based vector fields.

The volumes of the segmented volumes are shown in Figure 8. The 3.3 mm lesion could not be segmented with the used method in all four reconstructions. Compared to the actual lesion size, the segmented lesions in all reconstructions appear smaller. The simulated 7.5 mm lesion had a volume of 1.8 cc,

Table 3: Table containing the maximal displacements in each direction in all three lesions for the rCASPR-based simulation. (AP = Anterior-Posterior, LR = Left-Right, FH = Feet-Head).

	Lesion 1	Lesion 2	Lesion 3
Max. AP displacement	5.3 mm	5.5 mm	5.1 mm
Max. LR displacement	4.6 mm	4.3 mm	3.7 mm
Max. FH displacement	3.0 mm	4.5 mm	3.7 mm

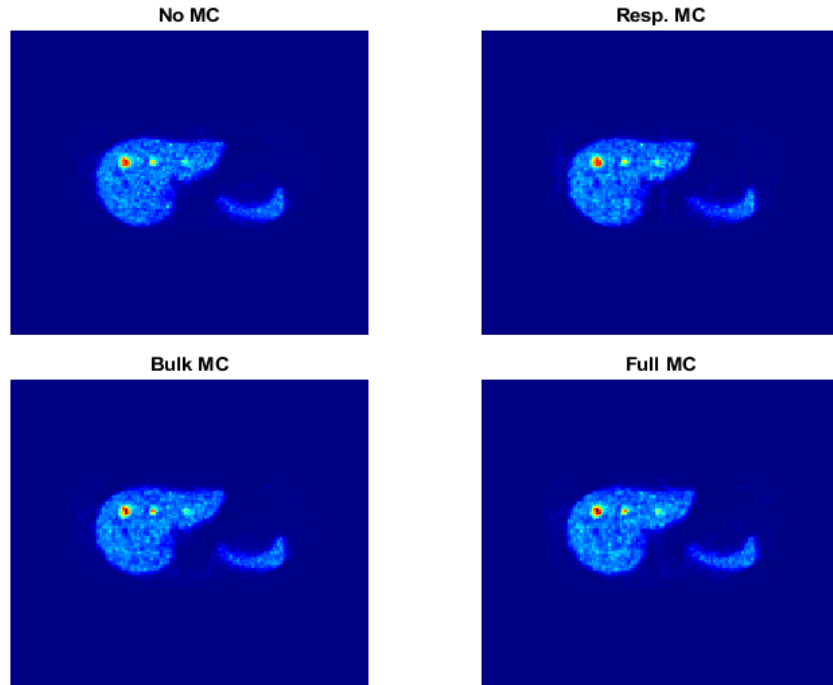


Figure 6: Visualization of the axial middle slice through the lesions for all four reconstructions. (MC = motion correction).

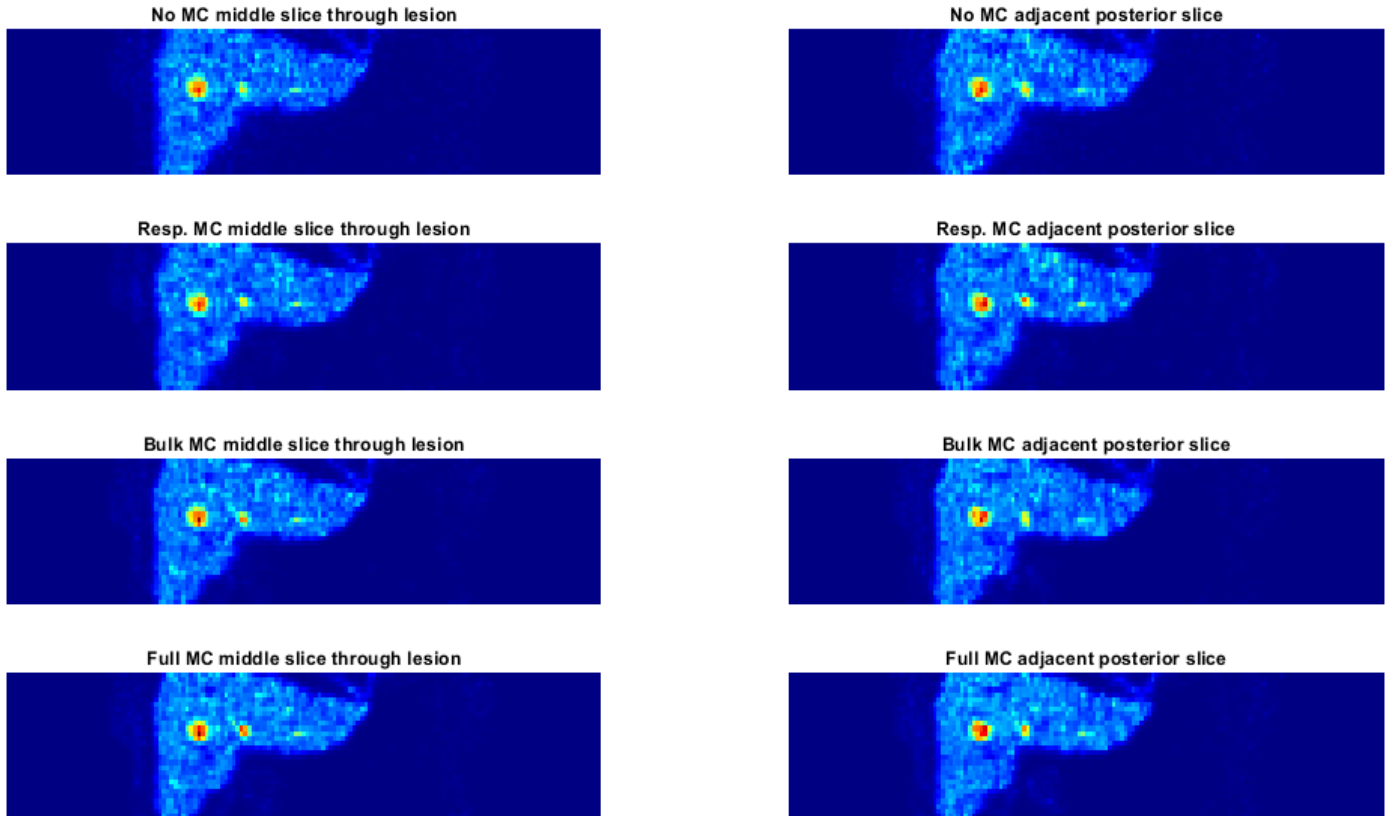


Figure 7: Coronal view of two adjacent slices of the four different reconstructions of the simulations with the rCASPR-based vector fields. (MC = motion correction).

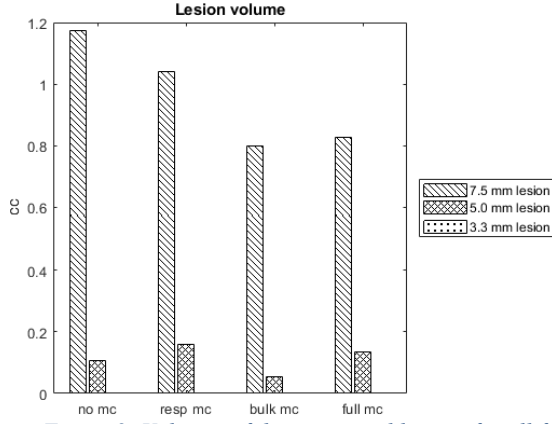


Figure 8: Volumes of the segmented lesions for all four reconstructions (mc = motion correction).

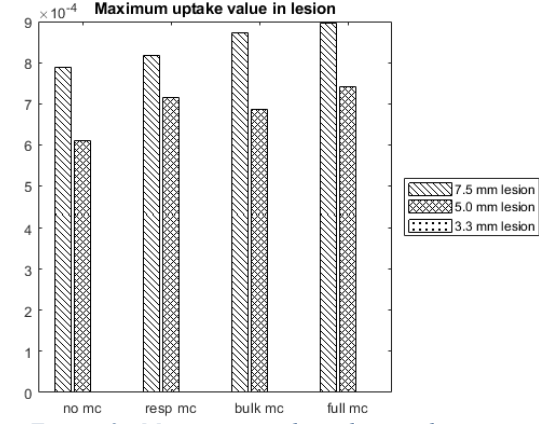


Figure 9: Maximum uptake value in the segmented lesions for all four reconstructions (mc = motion correction).

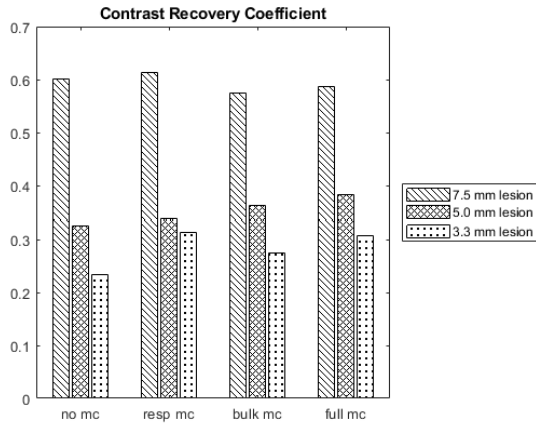


Figure 10: CRC of the spherical regions of interest for all four reconstructions (mc = motion correction).

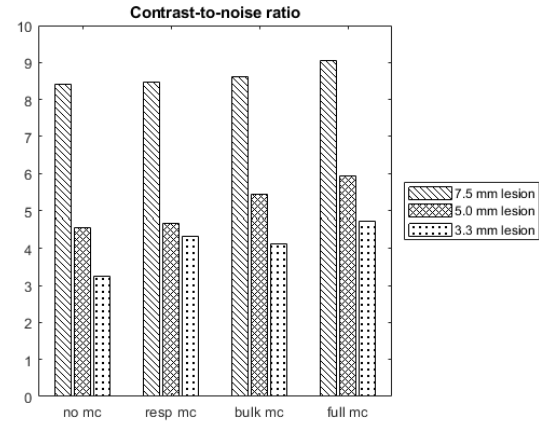


Figure 11: CNR of the spherical regions of interest for all four reconstructions (mc = motion correction).

the 5.0 mm lesion had a volume of 0.61 cc and the 3.3 mm lesion had a volume of 0.16 cc. The maximum uptake values in the segmented lesions are shown in Figure 9.

Figure 10 shows the CRC values of the spherical regions of interest. The CNR values for the spherical regions of interest are presented in Figure 11.

Overall, based on the quantitative analysis and comparing the values to the reconstruction with the full vector field, the reconstruction with bulk motion correction appears most similar and the reconstruction without motion correction appears least similar. However, for the two smaller lesions, the highest similarity to the full motion corrected reconstruction alternates between the bulk and respiratory motion corrected reconstructions.

The quantitative analysis shows that the detectability drops for smaller lesions (i.e. they have a lower maximum intensity, CRC and CNR).

V. DISCUSSION

The purpose of the experiments with the rCASPR-based vector fields was to study the feasibility of using rCASPR for motion correction on the PET/MRI system at the UMC Utrecht. Additionally, we were able to assess the relative importance of bulk versus respiratory motion correction.

By using a 1.5T Elekta Unity/Philips Marlin system for the acquisition of the vector fields, the acquisition is representative for possible acquisitions on the PET/MRI system, since it also features 1.5T magnet, a split gradient coil and an identical body coil. However, due to the integration with PET, another surface coil might be used on acquisitions with the PET/MRI system to minimize attenuation by the surface coil. Motion detection using the T_1 -weighted rCASPR sequence was successful and vector fields could be used for the PET simulations.

Due to time considerations, an analytical projector provided by the makers of CASToR was used for the generation of the PET data. The accuracy of this analytical projector has not been reported. For simulations known to be accurate, Monte Carlo simulations would be needed to generate the PET data, for example by using GATE (Jan et al., 2004). With GATE, it would also be possible to include the generation of accurate scatter events (including multiple scattered events), random events and time-of-flight (ToF) information, so all possible corrections could be included in reconstructions. In this study, random correction, detector efficiency normalization and ToF have not been used.

Compared to the simulated activity map of the phantom, the lesions segmented from the reconstructions appear smaller. This can be explained by a combination of using a relatively low-count acquisition and a threshold-based segmentation.

Because the rCASPR scan took 132 s, the same scan time was chosen for the simulation of the PET acquisition. Typically, PET studies are acquired in 180 s for each bed position. Performing the simulations of this study for an acquisition time of 180 s rather than 132 s would result in a higher number of counts. As explained by Moses (2011), low-count acquisitions deteriorate image quality, which reduces the visibility of small lesions. Not using ToF may have led to higher noise levels in the reconstructions.

When comparing the reconstructions to the full motion corrected reconstruction, most results are comparable to what can be found in literature. As summarized by Catana (2015), motion artifacts result in blurring of lesions, which leads to higher lesion volumes, lower uptake values and reduced detectability for small lesions. The reconstruction with full motion correction indeed has the highest maximum uptake value for the lesions and highest CNR. The 7.5 mm lesion appears larger in the reconstruction with respiratory motion correction and without motion correction, and comparable for the reconstruction with bulk motion correction. The impact of the different types of motion correction on the volume of the 5.0 mm lesion varies, possibly due to the size of the lesion which lowers the detectability. The higher CRC levels for the 7.5 mm lesion for the reconstruction with respiratory motion correction and without motion correction can be explained by noise in the data.

Furthermore, when comparing with the full motion corrected reconstruction, reconstruction with bulk motion correction seems to result in bigger improvements of image quality for this volunteer than respiratory motion correction. The quantification of the detected motion shows that most motion in the 7.5 mm lesion is detected in the anterior-posterior and left-right directions. The 5.0 mm lesion has similar displacements in all three directions. Respiratory motion estimation with rCASPR is done using self-navigation in the feet-head direction, so it can be expected that respiratory motion correction would work best when higher displacements in the feet-head direction are observed. Literature also reveals that the biggest displacement in respiratory motion is in the feet-head direction. The 5.0 mm lesion is subject to higher feet-head displacement compared to the 7.5 mm lesion. The quantitative analysis for the 5.0 mm lesion of the respiratory motion corrected reconstruction shows more similar results to the full motion corrected reconstruction, compared to the 7.5 mm lesion. Bulk motion correction shows similar results as full motion correction for the 7.5 mm lesion. Another reason why bulk motion results in more similar results for this volunteer can be the fact that respiratory motion is periodic while the observed bulk motion in this experiment was not. Therefore, without incorporation of respiratory motion correction, most events might still have come from the average position in the respiratory motion cycle of this volunteer, resulting in less extensive blurring. Note that these results are specific for this volunteer and might differ for other volunteers.

V. A. Future research

This study was part of the development of a PET/MRI system at the UMC Utrecht and focused on motion correction possibilities. One of the final goals of the development of the system is to obviate anesthesia in pediatric PET studies by

being able to track all types of motion. Although in this study both respiratory and bulk motion were corrected using rCASPR, it is not expected this method will be able to correct for more extensive repositioning. This is needed in pediatric PET studies when the patient has not been anesthetized. Therefore, other options for motion tracking should be studied, of which MR-MOTUS shows potential. This MR method generates vector fields directly from k -space data by comparing the measured k -space signal to the expected signal from a deformation field applied to a reference image. So far, it has shown to be able to correct for head-neck motion and respiratory motion, although not combined (Huttinga et al, 2020; Huttinga et al; 2021). Being model-based, this method can be presumed to be flexible. A logical next step would be to develop a model for MR-MOTUS which could be used to correct for combined respiratory and bulk motion, the predominant types of motion in pediatric PET studies.

As for the PET reconstruction, a logical next step would be to simulate PET acquisitions with Monte Carlo simulations in order to incorporate random correction and ToF. Reconstruction with multiple bed positions should be studied as well, since this might pose additional challenges to the current motion correction method.

Furthermore, challenges might be posed by the spatial distortion present in MR images at the edges of the transaxial and axial field of view, which is not present on PET images. This might complicate the registration of the attenuation map and the vector fields (Afaq et al., 2021). Experiments with a moving phantom might be used to investigate the impact of these distortions on the PET/MRI system.

V. B. Conclusions

The feasibility of using MR-based motion tracking with the rCASPR technique for motion correction of PET simulations was shown. Moreover, the relative impact of bulk motion correction versus respiratory motion correction could be assessed in the PET simulation containing both respiratory and bulk motion.

REFERENCES

- Afaq, A., Faul, D., Chebrolu, V. V., Wan, S., Hope, T. A., Haibach, P. V., & Bomanji, J. (2021, September). Pitfalls on PET/MRI. In *Seminars in Nuclear Medicine* (Vol. 51, No. 5, pp. 529-539). WB Saunders.
- Alessio, A., Kinahan, P. (2006). PET image reconstruction. *Nuclear medicine*, 1(1), 1-22.
- Bruijnen, T., Schakel, T., Akdag, O., Bruel, C. V. M., Lagendijk, J. J. W., van den Berg, C. A. T., & Tjissen, R. H. N. (2022). Free-breathing motion compensated 4D (3D+ respiration) T2-weighted turbo spin-echo MRI for body imaging. *arXiv preprint arXiv:2202.03021*.
- Catana, C. (2015). Motion correction options in PET/MRI. In *Seminars in nuclear medicine* (Vol. 45, No. 3, pp. 212-223). WB Saunders.
- Catana, C. (2018). PET/MRI: motion correction. In *PET/MRI in oncology* (pp. 77-96). Springer, Cham
- Cherry, S. R., Sorenson, J. A., & Phelps, M. E. (2012). *Physics in nuclear medicine e-Book*. Elsevier Health Sciences.
- Delso, G., & Nuyts, J. (2018). PET/MRI: attenuation correction. In *PET/MRI in Oncology* (pp. 53-75). Springer, Cham.

- Ehman, E. C., Johnson, G. B., Villanueva-Meyer, J. E., Cha, S., Leynes, A. P., Larson, P. E. Z., & Hope, T. A. (2017). PET/MRI: where might it replace PET/CT?. *Journal of Magnetic Resonance Imaging*, 46(5), 1247-1262.
- Huttinga, N. R., Van den Berg, C. A., Luijten, P. R., & Sbrizzi, A. (2020). MR-MOTUS: model-based non-rigid motion estimation for MR-guided radiotherapy using a reference image and minimal k -space data. *Physics in Medicine & Biology*, 65(1), 015004.
- Huttinga, N. R., Bruijnen, T., van den Berg, C. A., & Sbrizzi, A. (2021). Nonrigid 3D motion estimation at high temporal resolution from prospectively undersampled k -space data using low-rank MR-MOTUS. *Magnetic resonance in medicine*, 85(4), 2309-2326.
- Jan, S., Santin, G., Strul, D., Staelens, S., Assié, K., Autret, D., ... & Morel, C. (2004). GATE: a simulation toolkit for PET and SPECT. *Physics in Medicine & Biology*, 49(19), 4543.
- Jiang, W., Ong, F., Johnson, K. M., Nagle, S. K., Hope, T. A., Lustig, M., & Larson, P. E. (2018). Motion robust high resolution 3D free-breathing pulmonary MRI using dynamic 3D image self-navigator. *Magnetic resonance in medicine*, 79(6), 2954-2967.
- Kannan, S., Teo, B. K. K., Solberg, T., & Hill-Kayser, C. (2017). Organ motion in pediatric high-risk neuroblastoma patients using four-dimensional computed tomography. *Journal of applied clinical medical physics*, 18(1), 107-114.
- Klein, S., Staring, M., Murphy, K., Viergever, M. A., & Pluim, J. P. (2009). Elastix: a toolbox for intensity-based medical image registration. *IEEE transactions on medical imaging*, 29(1), 196-205.
- Marin, T., Djebra, Y., Han, P. K., Chemli, Y., Bloch, I., El Fakhri, G., ... & Ma, C. (2020). Motion correction for PET data using subspace-based real-time MR imaging in simultaneous PET/MR. *Physics in Medicine & Biology*, 65(23), 235022.
- Merlin, T., Stute, S., Benoit, D., Bert, J., Carlier, T., Comtat, C., ... & Visvikis, D. (2018). CASToR: a generic data organization and processing code framework for multi-modal and multi-dimensional tomographic reconstruction. *Physics in Medicine & Biology*, 63(18), 185005.
- Moses, W. W. (2011). Fundamental limits of spatial resolution in PET. *Nuclear Instruments and Methods in Physics Research Section A: Accelerators, Spectrometers, Detectors and Associated Equipment*, 648, S236-S240.
- Papathanassiou, D., Bruna-Muraille, C., Liehn, J. C., Nguyen, T. D., & Curé, H. (2009). Positron emission tomography in oncology: present and future of PET and PET/CT. *Critical reviews in oncology/hematology*, 72(3), 239-254.
- Segars, W. P., Sturgeon, G., Mendonca, S., Grimes, J., & Tsui, B. M. (2010). 4D XCAT phantom for multimodality imaging research. *Medical physics*, 37(9), 4902-4915.
- Shamonin, D. P., Bron, E. E., Lelieveldt, B. P., Smits, M., Klein, S., Staring, M., & Alzheimer's Disease Neuroimaging Initiative. (2014). Fast parallel image registration on CPU and GPU for diagnostic classification of Alzheimer's disease. *Frontiers in neuroinformatics*, 7, 50.
- Siemens Healthineers (2021). Deviceless motion management for PET imaging. Retrieved from: www.siemens-healthineers.com/oncofreeze
- Tong, S., Alessio, A. M., & Kinahan, P. E. (2010). Image reconstruction for PET/CT scanners: past achievements and future challenges. *Imaging in medicine*, 2(5), 529.
- Uh, J., Krasin, M. J., Li, Y., Li, X., Tinkle, C., Lucas Jr, J. T., ... & Hua, C. (2017). Quantification of pediatric abdominal organ motion with a 4-dimensional magnetic resonance imaging method. *International Journal of Radiation Oncology* Biology* Physics*, 99(1), 227-237.
- Van der Schagt, I. (2021). The feasibility of motion corrected PET/MRI with the purpose of obviating anesthesia for pediatric imaging.
- Watson, C. C. (2000). New, faster, image-based scatter correction for 3D PET. *IEEE Transactions on Nuclear Science*, 47(4), 1587-1594.
- Zachiu, C., Papadakis, N., Ries, M., Moonen, C., & De Senneville, B. D. (2015). An improved optical flow tracking technique for real-time MR-guided beam therapies in moving organs. *Physics in Medicine & Biology*, 60(23), 9003.
- Zaidi, H., Montandon, M. L., & Alavi, A. (2007). Advances in attenuation correction techniques in PET. *PET clinics*, 2(2), 191-217.

Appendix 1: Single scatter simulation for the PET/MRI system at the UMC Utrecht

I. THEORY

Single scatter simulation (SSS) is a method to predict the scatter rate at each line of response in a PET study given an attenuation map, activity map and PET geometry. Based on the attenuation map, the contour of the imaged object is defined and all points within this object are defined as scatter points. For all scatter points, a prediction can be made on the expected scatter contribution to the total amount of counts for each line of response in the PET system. This is done based on the formula

$$S^{AB} = \int_{V_S} dV_S \left(\frac{\sigma_{AS}\sigma_{SB}}{4\pi R_{AS}^2 R_{SB}^2} \right) \frac{\mu}{\sigma_c} \frac{d\sigma_c}{d\Omega} [I^A + I^B] \quad (\text{Eq. A1.1})$$

where the first term in the integral $\left(\frac{\sigma_{AS}\sigma_{SB}}{4\pi R_{AS}^2 R_{SB}^2} \right)$ denotes a geometrical correction. The second term $\frac{\mu}{\sigma_c} \frac{d\sigma_c}{d\Omega}$ denotes the probability for a scatter event to happen for a given scatter angle and photon energy, which can be calculated using the Klein-Nishina equation. I^A and I^B are represented by

$$I^A = \varepsilon_{AS}\varepsilon'_{SB} e^{-\left(\int_S^A \mu ds + \int_S^B \mu ds\right)} \int_S^A \lambda(s) ds \quad (\text{Eq. A1.2})$$

and

$$I^B = \varepsilon_{BS}\varepsilon'_{SA} e^{-\left(\int_S^A \mu ds + \int_S^B \mu ds\right)} \int_S^B \lambda(s) ds \quad (\text{Eq. A1.3}).$$

Here, the first two terms ($\varepsilon_{AS}\varepsilon'_{SB}$ or $\varepsilon_{BS}\varepsilon'_{SA}$) represent the detector efficiencies for the given photon trajectory. The third term ($e^{-\int_S^A \mu ds + \int_S^B \mu ds}$ or $e^{-\int_S^A \mu ds + \int_S^B \mu ds}$) is the total attenuation along the photon paths and the fourth term ($\int_S^A \lambda(s) ds$ or $\int_S^B \lambda(s) ds$) is the total activity along the photon paths. Using a tail-fitting method, the produced scatter sinogram can be scaled to the PET data and correction factors can be produced (Watson, 2000). A visual presentation of the SSS is shown in Figure A1.1.

II. IMPLEMENTATION

In this study, a version of this SSS method has been implemented for the PET/MRI system in the UMC Utrecht. Following Watson (2000), to have a fast implementation, the activity and attenuation map are cropped to a lower resolution and scatter points with a low attenuation coefficient (e.g. air) are neglected. The activity and attenuation map were cropped to a resolution of $9.1 \times 9.1 \times 9.9 \text{ mm}^3$. Furthermore, scatter rates for only 1.4% (3 rings out of 36 rings and 72 detectors out of 432 detectors per ring) of all detectors were calculated. Using linear interpolation, the scatter sinogram was brought to the same dimensions as the PET data. Tail fitting was done by

fitting the simulated scatter rates to the amount of events outside of the body contour.

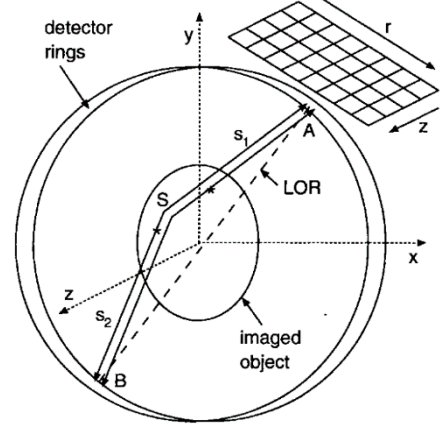


Figure A1.1: Visual presentation of the single scatter simulation for one scatter point and line of response. The scatter point is presented as S and the annihilation events with an asterisk (*). The detectors are placed at A and B in the ring-system (Watson et al., 1997).

III. INITIAL VALIDATION

An initial validation of the algorithm was done by comparing the produced scatter sinograms to scatter sinograms of a low-count Monte Carlo simulation of the same phantom with GATE (Jan et al., 2004). A visual comparison of the sinograms is shown in Figure A1.2. The goal in this initial validation was to have the SSS sinograms resembling the shape and intensity distribution of the Monte Carlo sinograms.

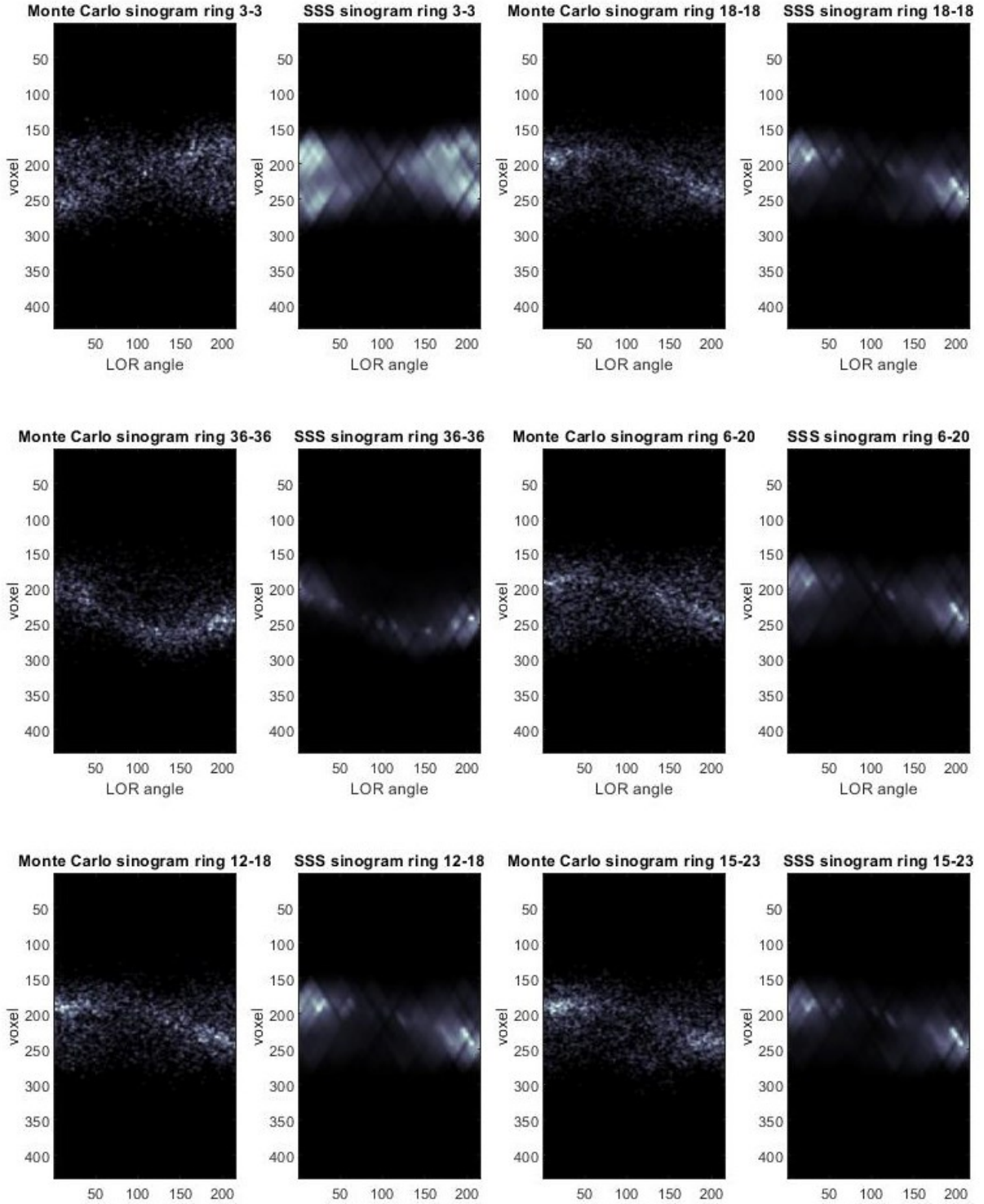
It should be noted that this initial validation cannot be seen as a proper validation of the algorithm. In order to do that, the output should be compared to a high-count Monte Carlo simulation and the effect of the scatter correction in the reconstruction should be studied as well.

ACKNOWLEDGEMENTS

I would like to thank R. Jose Santo for finalizing the SSS-algorithm and K. Vrakidis for providing the data and phantom of the Monte Carlo simulation.

REFERENCES

- Jan, S., Santin, G., Strul, D., Staelens, S., Assié, K., Autret, D., ... & Morel, C. (2004). GATE: a simulation toolkit for PET and SPECT. *Physics in Medicine & Biology*, 49(19), 4543.
- Watson, C. C., Newport, D., Casey, M. E., DeKemp, R. A., Beanlands, R. S., & Schmand, M. (1997). Evaluation of simulation-based scatter correction for 3-D PET cardiac imaging. *IEEE Transactions on Nuclear Science*, 44(1), 90-97.
- Watson, C. C. (2000). New, faster, image-based scatter correction for 3D PET. *IEEE Transactions on Nuclear Science*, 47(4), 1587-1594.



Figuur A1.2: Visual comparison between the simulated scatter rates by the single scatter simulation (SSS) algorithm for the PET/MRI system at the UMC Utrecht and the scatters simulated with a low-count Monte Carlo simulation of the same phantom. This comparison serves as an initial validation of the algorithm and the goal was to let the SSS sinograms resemble the Monte Carlo sinograms in terms of shape and intensity distribution. Both non-oblique (both detectors in same ring) and oblique (detectors in two different rings) sinograms are shown. The SSS and Monte Carlo sinograms are shown in pairs. The Monte Carlo sinograms were blurred with a Gaussian filter.